NANO LETTERS

Letter

pubs.acs.org/NanoLett

Resonant Tunneling through Discrete Quantum States in Stacked Atomic-Layered MoS_2

Linh-Nam Nguyen,[†,‡] Yann-Wen Lan,*[,†,§] Jyun-Hong Chen,[∥] Tay-Rong Chang,[⊥] Yuan-Liang Zhong,[∥] Horng-Tay Jeng,[†,⊥] Lain-Jong Li,[§] and Chii-Dong Chen*[,†]

[†]Institute of Physics, Academia Sinica, Taipei 11529, Taiwan

[‡]Danang College of Technology, The University of Danang, Danang 59000, Vietnam

[§]Institute of Atomic and Molecular Science, Academia Sinica, Taipei 11529, Taiwan

[∥]Department of Physics and Center for Nanotechnology, Chung Yuan Cristian University, Chungli 32023, Taiwan

[⊥]Department of Physics, National Tsing Hua University, Hsinchu 30013, Taiwan

Supporting Information

ABSTRACT: Two-dimensional crystals can be assembled into three-dimensional stacks with atomic layer precision, which have already shown plenty of fascinating physical phenomena and been used for prototype vertical-field-effect-transistors.[1,2] In this work, interlayer electron tunneling in stacked high-quality crystalline MoS_2 films were investigated. A trilayered MoS_2 film was sandwiched between top and bottom electrodes with an adjacent bottom gate, and the discrete energy levels in each layer could be tuned by bias and gate voltages. When the discrete energy levels aligned, a resonant tunneling peak appeared in the current−voltage characteristics. The peak position shifts linearly with perpendicular magnetic field, indicating formation of Landau levels. From this linear dependence, the effective mass and Fermi velocity are determined and are confirmed by electronic structure calculations. These fundamental parameters are useful for exploitation of its unique properties.

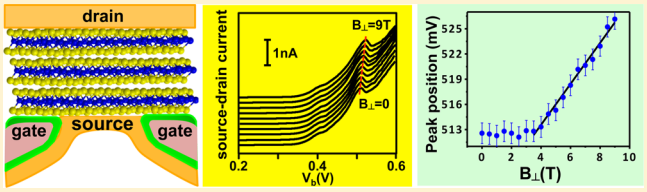

KEYWORDS: *Metal transition dichalcogenide, MoS_2, interlayer electron transport, resonant tunneling, discrete energy levels, nanopore structure*

Molybdenum disulfide (MoS_2) is a prototypical transition metal dichalcogenide. It has a layered structure wherein molybdenum atoms are sandwiched between the layers of sulfur atoms in a hexagonal arrangement. Atomic MoS_2 sheet is a semiconductor with large bandgap. Similar to graphene, single layer MoS_2 possesses unique properties such as high transparent and two-dimensional (2D) flexible geometry and has become an emerging material in the field of nanoelectronics.[3−16] In multilayer structures, the interlayer interaction can play an important role in determining electronic properties. In the case of few-layer graphene, the interlayer coupling can modify the subband curvature, leading to the opening of a subband spacing or energy gap.[17−21] Experimental studies on the interlayer electron transferring in graphene systems were conducted and exhibited interesting transport behavior.[22,23] In the case of multilayer MoS_2, the interlayer coupling arises from overlapping of electron wave function due to the small separation between sulfide sheets. Consequently, the bandgap of the multilayer structure is predicted to be tunable by an electric field.[24] Although lateral transport properties of few-layer MoS_2 have been studied experimentally,[8−15] perpendicular-to-plane electrical transport has not been investigated. Experimental study on interlayer electron transferring in MoS_2 systems should reveal useful information needed for the development of multilayered electronics.

In this work, we report perpendicular electron transport through a highly crystalline trilayer MoS_2 structure in nanometer area. The interlayer tunneling current was found to be modulated by transverse electric fields as well as perpendicular magnetic fields. Our experiment provided evidence of inter-MoS_2 layer charge tunneling and suggested a wave function overlap between the sulfide atomic layers of the two stacked MoS_2 layers. Furthermore, the current−voltage (I−V_b) characteristics exhibited a resonant peak structure, suggesting presence of quantized energy levels in the MoS_2 sheets. The peak position shifted linearly with the perpendicularly applied magnetic field, indicating formation of Landau levels. From this dependence, the effective mass and Fermi velocity were determined. The effective mass was found to be much smaller than the predicated value for single MoS_2 layers. Electronic structure calculation was performed to confirm the experimental results.

High quality atomic-layered MoS_2 films were synthesized by the following processes.[25] Cleaned sapphire substrates were immersed into 1.25 wt % of $(NH_4)_2MoS_4$ and dimethylformamide (DMF) solution and then slowly pulled out to form thin

Received: December 26, 2013
Revised: April 14, 2014
Published: April 18, 2014

$(NH_4)_2MoS_4$ films on the substrate surface. In general, few-layer MoS_2 sheets could be obtained using diluted precursor solution and with a fast dip-coating process. Residual solvents and other contaminations were removed in 1 Torr Ar/H_2 gas mixture (flow rate ratio = 4:1) at for 500 °C for 1 h. Subsequently, the specimen were subjected to a second annealing process in 500 Torr Ar/S gas mixture at 1000 °C for 30 min. The added sulfur helped to improve the crystalline of layered MoS_2 films. In the optimized synthesis condition, large and homogeneous MoS_2 trilayers could be produced across the entire chip with a repeatability of about 90%. Figure 1a shows a transmission electron microscopy (TEM) image of

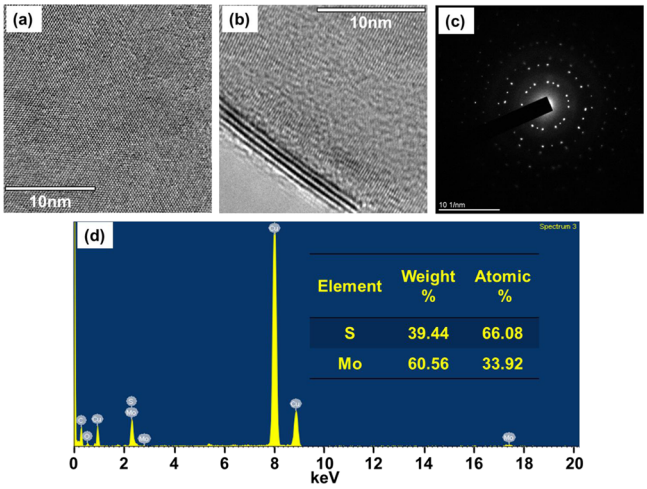

Figure 1. TEM inspections of the synthesized trilayer MoS_2 on grids. (a,b) High-resolution TEM images. (b) TEM image is taken at the film curled edge and shows clearly the three layer structure. (c) The SAED pattern. The SAED aperture size is 250 nm in diameter. (d) TEM-EDS analysis of the composition ratio. The TEM inspections clearly show that the trilayer MoS_2 sheets have large domain size with high crystalline.

the synthesized MoS_2 sheets, which reveals periodic atom arrangement of highly crystalline trilayer MoS_2 films. As shown in Figure 1b, the three layers can be clearly identified in the curled edge of a free-hanging trilayer. Figure 1c displays the selected area electron diffraction (SAED) pattern showing three sets of hexagonal lattice structure, indicating that misorientation may exist at some places. Diffraction patterns (not shown) indicated that the crystalline domain size is greater than 250 nm. It is also noted from TEM-based energy dispersive spectroscopy (TEM-EDS) analysis (Figure 1d) that the atomic percentage ratio between Mo and S is 1:2.

The trilayer MoS_2 films were then made into electronic devices by using the following procedures. Silicon nitride (Si_3N_4) membrane chips with millimeter-sized Au contact pad on the front-side for electrical measurements were made on 500 μm thick silicon substrates by standard photolithography and anisotropic KOH etching. Electron-beam lithography and reactive-ion etching were then employed to create a nanopore on the membrane. The pore was then surrounded by a 24 nm thick aluminum (Al) gate-electrode, which is covered by an 8 nm thick aluminum oxide (Al_2O_3) insulating layer. Because of these coating layers, the diameter of final pore on the Si_3N_4 membrane shrank. As shown in the inset of Figure 2a, the diameter of pore in Device 1 is about 28 nm. The diameters of pores in Device 2 and 3 are 44 and 72 nm, respectively, as

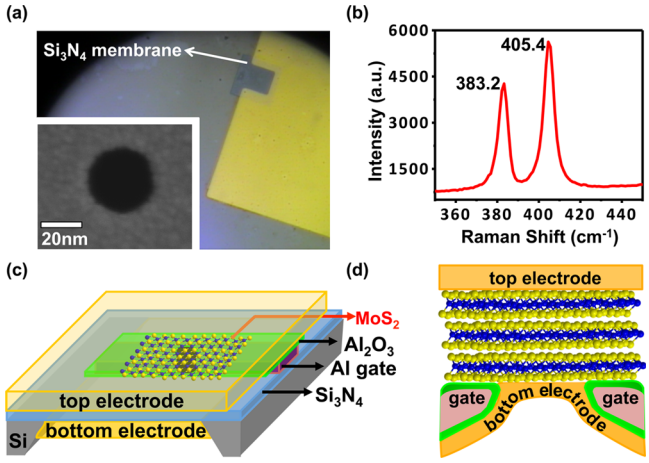

Figure 2. (a) Optical microscopy image of a Si_3N_4 membrane chip coated with transferred trilayer MoS_2. The inset is an SEM image of Device 1 showing a nanopore made on Si_3N_4 membrane. (b) Raman spectra for the transferred trilayer MoS_2 on the membrane. (c) Schematic illustration of the nanopore device with the trilayer MoS_2 sandwiched between the top and bottom electrodes. (d) A cross-sectional drawing of the trilayer MoS_2 device structure at the nanopore area.

shown in Supporting Information. The as-grown trilayer MoS_2 was then transferred to the top of nanopore on membrane. Prior to the transferring, the sapphire-caped trilayer MoS_2 sheets were spin-coated with PMMA and then immersed into NaOH solution to etch away sapphire. The PMMA-caped MoS_2 was first cleaned by deionized water and placed on membrane surface to cover the nanopore. After removing PMMA, the trilayer MoS_2 surface was further cleaned by chloroform. Figure 2b displays Raman spectra of the transferred MoS_2 film at the membrane area. The film exhibits two Raman characteristic peaks at 383.2 and 405.4 cm^{-1}, corresponding to E^1_{2g} and A_{1g} modes, respectively. The energy difference between two peaks is 22.2 cm^{-1}, indicating that the MoS_2 film has trilayer structure,[25,26] as reported in the TEM analysis in Figure 1. After transferring of the trilayer MoS_2, Au/Ti films are subsequently thermally evaporated onto the both sides of the chip to form top and bottom electrodes. Ti is chosen as the contact metal because the work function of Ti (~4.3 eV) is very close to the electron affinity of thin-layer MoS_2 (~4.2 eV),[27] and a good Ohmic contact between them is expected. As schematically illustrated in Figure 2c,d, the completed device consists of a trilayer-MoS_2 laid on top of the gated nanopore and sandwiched between top and bottom electrodes. The overlapping of electron wave functions between layered MoS_2 enables interlayer charge transfer, just like that in few-layer graphene.[17−21] Under a bias source-drain voltage V_b, this charge transfer yield a perpendicular current I. This perpendicular current through the trilayer MoS_2 will be confined on one side by a nanopore on a Si_3N_4 membrane. In addition, capacitive coupling exists between the bottom gate electrode and each MoS_2 layers. This coupling enables gate-modulation of the carrier concentration in MoS_2 layers, making the device a vertical field-effect-transistor. Details of nanopore fabrication procedure and transfer process can be found in ref 28 and in Supporting Information (Figure S1). All the low-temperature electrical measurements were carefully conducted using a homemade current−voltage amplifier with completely symmetric circuit for best common-mode noise rejection.

dx.doi.org/10.1021/nl404790n | Nano Lett. 2014, 14, 2381−2386

On the basis of the device geometry shown in Figure 2d, a circuit model displayed in Figure 3a is proposed, in which the

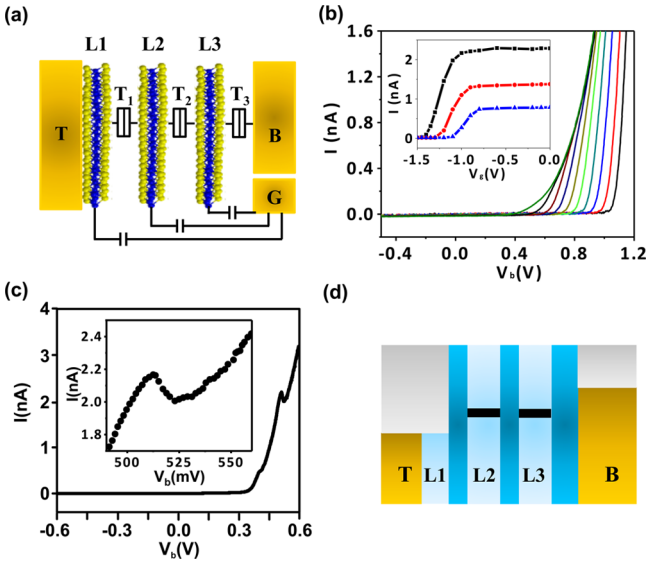

Figure 3. (a) The proposed model of the gated-trilayer MoS_2 device sandwiched between top (T) and bottom (B) electrodes. (b) $I-V_b$ curves of Device 3 at gate voltages varying from −1.5 V (left-most green curve) to −0.5 V (right-most black curve) with a step of 0.1 V at 60 K. Inset shows $I-V_g$ characteristics at V_b = 1 V (black), 0.9 V (red), and 0.8 V (blue), indicating that the MoS_2 trilayer is of n-type. (c) $I-V_b$ curve of Device 1 at gate voltage of 0.1 V measured at 3 K. The inset displays a magnified $I-V_b$ at resonant tunneling peak around 512 mV. The very smeared current plateau at $V_b \sim 400$ mV can probably be explained by tunneling through broadened levels. (d) Schematic illustration of the potential diagram for the energy level alignment at which the current reaches maximum value. As gate or drain voltage is tuned away, these energy levels are not aligned and the tunneling current decreases.

three MoS_2 layers from top to bottom are denoted as L1, L2, and L3. As illustrated in Figure 2d, the top contact area between Ti/Au and MoS_2 is about 40 000 times larger than that of the bottom contact; the latter is defined by the nanopore window. This difference in the contact area results in a large difference in the contact resistance. This, together with the gated transistor circuit, gives rise to the rectification current−voltage ($I-V_b$) characteristics shown in Figures 3b and 3c. Similar types of structure-asymmetry induced rectification behavior are reported for not only nanopore devices,[28,29] but also nanowire devices with different contact areas.[30,31] Figure 3b and the inset show gate modulation of current, clearly displaying n-type behavior. Throughout this work, the carrier concentration in MoS_2 layers is depleted to a low value by setting the gate to a voltage slightly above the threshold voltage. With this low carrier concentration, the electric coupling between the gate electrode and L2 is not to be shielded by L1. An $I-V_b$ characteristic is displayed in Figure 3c, and a close view of the $I-V_b$ characteristic (see the inset) reveals a current peak in the forward bias regime at V_b = 512 mV at a temperature of 3 K. We attribute this peak structure to the resonant charge tunneling through quantized energy levels in a double-quantum-well device, similar to those in Ge/Si[32] and Si/Si_xGe_{1-x}[33] multilayer heterostructures. In our devices, the level quantization in the quantum wells is originated from the electron wave function confined in a two-dimensional disc of atomic-layered MoS_2. The disc has a size corresponding to the size of the nanopore. Outside the nanopore, we postulate that the interaction between MoS_2 layer and underneath Al_2O_3/Si_3N_4 membrane deforms the electronic structure of MoS_2,[34,35] generating a disrupted potential profile. This effectively isolates the MoS_2 carriers in the nanopore area and discrete energy levels are formed. In the later part of this paper, this postulation will be confirmed experimentally, and we further show that the energy level spacing is much greater than the corresponding thermal energy of the measurement temperature.

While the energy levels are well-separated in L2, they are very much smeared in L1 due to its good electric contact to the top electrode. In L3, the contact area is small and the discrete levels are persevered because of the weak coupling to the bottom electrode. This coupling yields a route for electron tunneling, similar to those reported for metal/semiconductor nanocontacts.[36−38] Consequently, the trilayer devices are modeled as two quantum wells connected to top/bottom electrodes through three tunnel junctions (named as T1, T2, and T3), as illustrated in Figure 3a. In this model, the discrete levels in L2 and L3 in the bias window (between the Fermi levels of top and bottom electrodes) are involved in the transferring process, and their positions are determined by the capacitance values of the three tunnel junctions and their respective gate capacitances. In addition, from the cross-sectional drawing of the device shown in Figure 2d, we can assume that the capacitance values between the bottom gate electrode and the three MoS_2 layers are different, and by tuning the gate voltage these discrete levels are shifted differently. In a set of (V_b, V_g) values, as shown in Figure 3d, one of the discrete levels within the bias window in L2 can come into align with a level in L3, and the tunneling current is at a maximum in both V_b and V_g windows, which is the origin of resonant tunneling. As shown in Figure 4a, away from this set of (V_b, V_g), the levels

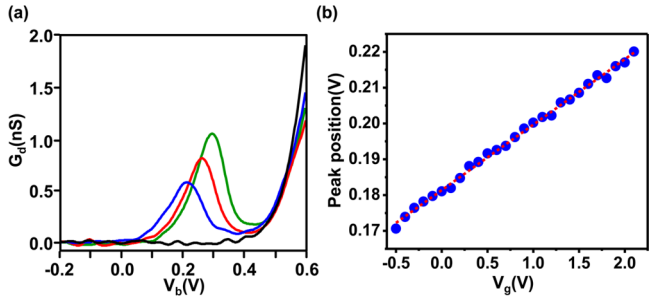

Figure 4. (a) G_d versus V_b curves of Device 3 at gate voltages of −0.7 V (black, bottom), −0.4 V (blue), 2 V (red), and 3 V (green, top) at 30 K. (b) Resonant peak position (in V_b) as a function of gate voltage. Red dashed line is a guide to the eye.

are not aligned and the differential conductance $G_d = dI/dV_b$ drops. Shown in Figure 4b is the linear shift of the conductance peak position with respect to V_b and V_g values. This linear shift is commonly observed in resonant tunneling transistors.[39,40]

Figure 5a and the inset show how the resonant peak shifts in the presence of perpendicular magnetic fields, which is a manifestation of Landau level shift[32,33] given by $\Delta E = \hbar\omega_c = e\hbar B/m^*$, where e, $\hbar$, B, ω_c and m^* are the elementary charge, Planck's constant, magnetic field, cyclotron frequency, and the effective mass, respectively. As displayed in Figure 5b for Device 1, for magnetic fields higher than 3.5 T the resonant peak position shifts linearly with magnetic field. From this

dx.doi.org/10.1021/nl404790n | Nano Lett. 2014, 14, 2381−2386

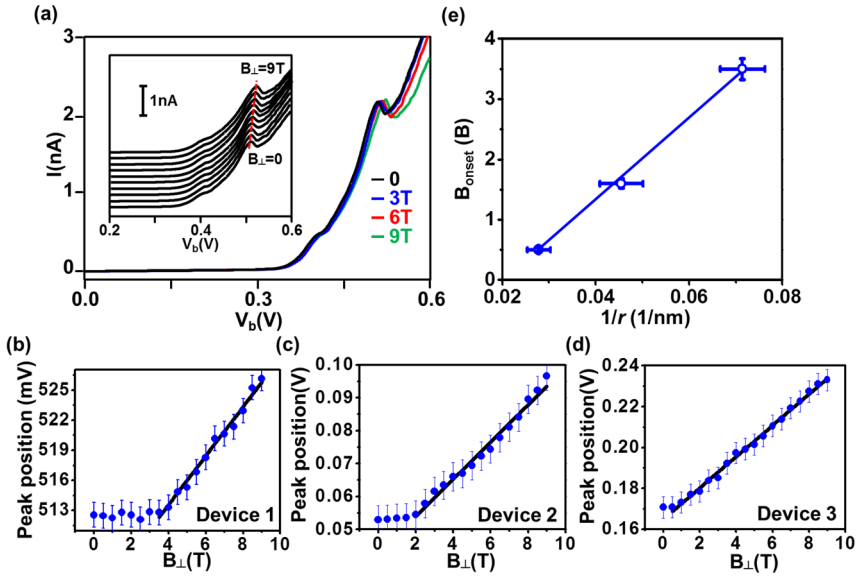

Figure 5. (a) $I-V_b$ characteristics of Device 1 in magnetic field ranging from 0 to 9 T with a step of 3 T. Inset shows the same curves with a step of 1 T. Each curve is shifted up by 0.2 nA for clarity. (b–d) Resonant peak position as a function of magnetic field with a linear fit for Devices 1 (b), 2 (c), and 3 (d). (e) Onset magnetic field plotted for three pore-radius, displaying a linear dependence of B_{onset} on $1/r$.

Table 1. Parameters Summarized for Three Devices

device #	pore radius (nm)	onset magnetic field (T)	effective mass	cyclotron frequency (rad/s)	fermi velocity (m/s)
1	14 ± 1	3.5 ± 0.175	(0.047 ± 0.002)m_e	(1.31 ± 0.09) × 10^{13}	(0.183 ± 0.018) × 10^6
2	22 ± 2	1.6 ± 0.08	(0.021 ± 0.0005)m_e	(1.34 ± 0.07) × 10^{13}	(0.295 ± 0.03) × 10^6
3	36 ± 3	0.5 ± 0.025	(0.015 ± 0.0003)m_e	(0.75 ± 0.04) × 10^{13}	(0.27 ± 0.027) × 10^6

linear dependence, the effective mass is determined to be 0.047 m_e with m_e the electron rest mass. The onset magnet field (B_{onset} = 3.5 T) corresponds to the largest circle that allows formation of cyclotron motion, which has a cyclotron frequency $\omega_{c,min}$ of 1.31 × 10^{13} rad/s. In view of our nanopore structure, it is reasonable that the cyclotron motion can exist only inside the nanopore. Outside the pore, the cyclotron motion is quenched by the interaction between MoS_2 and underneath Al_2O_3 insulating layer. By assuming a cyclotron radius r_c equal to the nanopore radius (14 nm for Device 1), the Fermi velocity $\nu_F = r_c\omega_{c,min}$ is determined to be 0.183 × 10^6 m/s. As shown in Figure 5c,d, Devices 2 and 3 also exhibit similar linear dependence of resonant peak position on magnetic field. The corresponding G_d-V_b curves are shown in Supporting Information (Figure S2). On the basis of the above analysis, ν_F, $\omega_{c,min}$ and m^* for all three devices are summarized in Table 1. The extracted Fermi velocity ν_F is somewhat smaller than the reported theoretical value of 0.53 × 10^6 m/s for MoS_2 monolayers[41] but is on the same order. Furthermore, it is found that the values of effective mass for three devices deviate from each other. This deviation can possibly be attributed to the nearest-neighbor intra-atoms coupling arising from layer misorientation or crystal distortion;[42] the latter may take place in the MoS_2 handling processes. Nevertheless obtained effective mass values are all on the same order and the average value is about 0.028 m_e. On the other hand, the onset magnetic field is related to the pore radius as $B_{onset} = [m^*\nu_F/e\hbar][1/r]$, and this linear dependence is confirmed in Figure 5(e). The $m^*\nu_F$ product can be extracted from the slope in $B_{onset} - 1/r$ plot. Provided that ν_F is known, this would be an independent approach for determination of m^*. By taking the theoretical value of ν_F, the effective mass value is found to be 0.022 m_e, which is in reasonable agreement with the average value of 0.028 m_e obtained from Table 1. Despite of this consistency, we note that these experimental values are one order smaller than the theoretical value of 0.5 m_e for MoS_2 monolayers.[43] To support the obtained experimental values first-principle calculations for effective mass in MoS_2 trilayers are performed, and the results are described in the Supporting Information. The calculated average Fermi velocities are 0.19 × 10^6 and 0.15 × 10^6 m/s, respectively, whereas the effective masses are estimated to be about 0.047 and 0.032 m_e, respectively. These values fully support our experimental findings. Also notice that the calculated $m^*\nu_F$ products are about 0.007 (in unit of m_e·m/s), which agree reasonably with the experimental value of 0.011 obtained from the slope in Figure 5e.

With the knowledge of the effective mass, the mean energy level spacing estimated by $\Delta\varepsilon = (1/\pi)(\hbar^2/m^*)(\pi^2/\pi r^2) = (\hbar^2/m^*r^2)$ for devices 1, 2, and 3 are about 8 meV (137 K), 3.24 mV (56 K) and 1.2 mV (21 K), respectively. These values are much greater than the thermal energy at 3 K, ensuring tunneling through a discrete level. The randomly embedded charge traps in the Al_2O_3/MoS_2 interface generate strong potential fluctuations,[34] which lead to localization of carriers in the MoS_2 outside the nanopore, giving rise to insulating behavior at low temperatures.[35] Because the free carriers are confined in the nanopore area, the energy levels are quantized. At temperatures higher than 40 K the conductive behavior in the MoS_2 outside the pore is recovered, and the carriers inside the pore area are thus delocalized. This transition from low-temperature localized state to high-temperature extended state can be clearly seen in Figure 6 in which the resonant peaks from 10 to 40 K are gradually smeared. As shown in Figure S3 in Supporting Information, similar behaviors were observed in

dx.doi.org/10.1021/nl404790n | Nano Lett. 2014, 14, 2381–2386

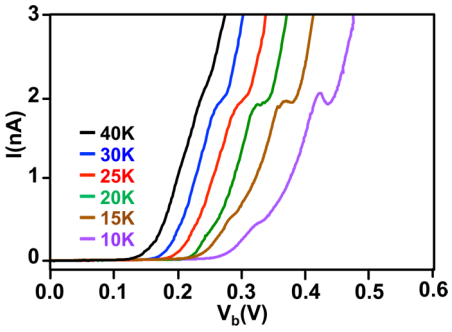

Figure 6. $I-V_b$ characteristics at temperatures from 40 K (black curve) to 10 K (purple curve) with a step of 5 K in Device 1. Note that the resonant peaks become apparent at low temperatures.

Devices 2 and 3. Furthermore, because the MoS_2 trilayer are likely to stack with random orientations (see Figure 1c), the wave-vector of tunneling electrons may vary from one layer to the other due to different orientations in the two-dimensional Brillouin Zone. The requirement that transverse momentum of tunneling electrons has to be conserved in the resonant tunneling process implies that the momentum-conserved interlayer transport can take place at different *k*-points of the two involving layers.

In conclusion, interlayer resonant tunneling between high-quality MoS_2 sheets was investigated. In the presence of a high-perpendicular magnetic field, the resonant tunneling peak position shifts linearly with the field strength, indicating formation of Landau levels. From the onset field and the slope of this linear dependence, Fermi velocity and the effective mass were determined, respectively, and these values were confirmed by band-structure calculations. The information from this expedition will pave the way for the development of MoS_2 electronics.

■ ASSOCIATED CONTENT

Ⓢ Supporting Information

Procedures for transferring as-grown MoS_2 sheets, additional transport characteristics for Devices 2 and 3, and band structure calculation for MoS_2 trilayer are provided. This material is available free of charge via the Internet at http://pubs.acs.org.

■ AUTHOR INFORMATION

Corresponding Authors

*E-mail: chiidong@phys.sinica.edu.tw (C.-D.C.).
*E-mail: ywlan@phys.sinica.edu.tw (Y.-W.L.).

Notes

The authors declare no competing financial interest.

■ ACKNOWLEDGMENTS

We thank Tzu-Hui Hsu and Shui-Jin Lai for their assistance during the course of this work. Fruitful discussions with Professors Ting-Kuo Lee and Mei-Yin Chou are highly appreciated. This research was funded by the National Science Council of Taiwan under contract No. NSC 101-2112-M-001-028-MY3. T.R.C. and H.T.J. are supported by the National Science Council, Taiwan under contract No. NSC 100-2112-M-007-024-MY3. H.T.J. also thanks NCHC, CINC-NTU and NCTS, Taiwan, for support in computer facilities. Technical support from NanoCore, the Core Facilities for Nanoscience and Nanotechnology at Academia Sinica, is acknowledged.

■ REFERENCES

(1) Britnell, L.; Gorbachev, R. V.; Jalil, R.; Belle, B. D.; Schedin, F.; Mishchenko, A.; Georgiou, T.; Katsnelson, M. I.; Eaves, L.; Morozov, S. V.; Peres, N. M. R.; Leist, J.; Geim, A. K.; Novoselov, K. S.; Ponomarenko, L. A. Field-Effect Tunneling Transistor Based on Vertical Graphene Heterostructures. *Science* **2012**, *335*, 947.

(2) Georgiou, T.; Jalil, R.; Belle, B. D.; Britnell, L.; Gorbachev, R. V.; Morozov, S. V.; Kim, Y. J.; Gholinia, A.; Haigh, S. J.; Makarovsky, O.; Eaves, L.; Ponomarenko, L. A.; Geim, A. K.; Novoselov, K. S.; Mishchenko, A. Vertical field-effect transistor based on graphene–WS_2 heterostructures for flexible and transparent electronics. *Nat. Nanotechnol.* **2013**, *8*, 100–103.

(3) Feldman, Y.; Wasserman, E.; Srolovitz, D. J.; Tenne, R. High-Rate, Gas-Phase Growth of MoS_2 Nested Inorganic Fullerenes and Nanotubes. *Science* **1995**, *267*, 222.

(4) Splendiani, A.; Sun, L.; Zhang, Y.; Zhang, Y.; Li, T.; Kim, J.; Chim, J. F.; Galli, G.; Wang, F. Emerging Photoluminescence in Monolayer MoS_2. *Nano Lett.* **2010**, *10*, 1271–1275.

(5) Mak, K. F.; Lee, C.; Hone, J.; Shan, J.; Heinz, T. F. Atomically Thin MoS_2: A New Direct-Gap Semiconductor. *Phys. Rev. Lett.* **2010**, *105*, 136805.

(6) Li, H.; Zhang, Q.; Yap, C. C. R.; Tay, B. K.; Edwin, T. H. T.; Olivier, A.; Baillargeat, D. From Bulk to Monolayer MoS_2: Evolution of Raman Scattering. *Adv. Funct. Mater.* **2012**, *22*, 1385–1390.

(7) Castellanos-Gomez, A.; Barkelid, M.; Goossens, A. M.; Calado, V. E.; van der Zant, H. S. J.; Steele, G. A. Laser-Thinning of MoS_2: On Demand Generation of a Single-Layer Semiconductor. *Nano Lett.* **2012**, *12*, 3187–3192.

(8) Radisavljevic, B.; Radenovic, A.; Brivio, J.; Giacometti, V.; Kis, A. Single-layer MoS_2 transistors. *Nat. Nanotechnol.* **2011**, *6*, 147–150.

(9) Yin, Z.; Li, H.; Li, H.; Jiang, L.; Shi, Y.; Sun, Y.; Lu, G.; Zhang, Q.; Chen, X.; Zhang, H. Single-layer MoS_2 phototransistors. *ACS Nano* **2012**, *6*, 74–80.

(10) Zhang, Y.; Ye, J.; Matsuhashi, Y.; Iwasa, Y. Ambipolar MoS_2 Thin FlakeTransistors. *Nano Lett.* **2012**, *12*, 1136–1140.

(11) Radisavljevic, B.; Whitwick, M. B.; Kis, A. Integrated Circuits and Logic Operations Based on Single-Layer MoS_2. *ACS Nano* **2011**, *5*, 9934–9938.

(12) Yoon, Y.; Ganapathi, K.; Salahuddin, S. How Good Can Monolayer MoS_2 Transistors Be? *Nano Lett.* **2011**, *11*, 3768–3773.

(13) Pu, J.; Yomogida, Y.; Liu, K. K.; Li, L. J.; Iwasa, Y.; Takenobu, T. Highly Flexible MoS_2 Thin-Film Transistors with Ion Gel Dielectrics. *Nano Lett.* **2012**, *12*, 4013–4017.

(14) Wu, S.; Zeng, Z.; He, Q.; Wang, Z.; Wang, S. J.; Du, Y.; Yin, Z.; Sun, X.; Chen, W.; Zhang, H. Electrochemically Reduced Single-Layer MoS_2 Nanosheets: Characterization, Properties, and Sensing Applications. *Small* **2012**, *8*, 2264–2270.

(15) Wang, H.; Yu, L.; Lee, Y. H.; Shi, Y.; Hsu, A.; Chin, M. L.; Li, L. J.; Dubey, M.; Kong, J.; Palacios, T. Integrated Circuits Based on Bilayer MoS_2 Transistors. *Nano Lett.* **2012**, *12*, 4674–4680.

(16) Kaasbjerg, K.; Thygesen, K. S.; Jacobsen, K. W. Phonon-limited mobility in n-type single-layer MoS_2 from first principles. *Phys. Rev. B* **2012**, *85*, 115317.

(17) Castro Neto, A. H.; Guinea, F.; Peres, N. M. R.; Novoselov, K. S.; Geim, A. K. The electronic properties of grapheme. *Rev. Mod. Phys.* **2009**, *81*, 109.

(18) Li, Z. Q.; Henriksen, E. A.; Jiang, Z.; Hao, Z.; Martin, M. C.; Kim, P.; Stormer, H. L.; Basov, D. N. Band Structure Asymmetry of Bilayer Graphene Revealed by Infrared Spectroscopy. *Phys. Rev. Lett.* **2009**, *102*, 037403.

(19) Sui, Y.; Appenzeller, J. Screening and Interlayer Coupling in Multilayer Graphene Field-Effect-Transistors. *Nano Lett.* **2009**, *9*, 2973–2977.

(20) Zhang, Y.; Tang, T. T.; Girit, C.; Hao, Z.; Martin, M. C.; Zettl, A.; Crommie, M. F.; Shen, Y. R.; Wang, F. Direct observation of a widely tunable bandgap in bilayer graphene. *Nature* **2009**, *459*, 820.

(21) Ramasubramaniam, A. Tunable Band Gaps in Bilayer Graphene-BN Heterostructures. *Nano Lett.* **2011**, *11*, 1070–1075.

(22) Lee, Y. H.; Kim, Y. J.; Lee, J. H. Vertical conduction behavior through atomic graphene device under transverse electric field. *Appl. Phys. Lett.* **2011**, *98*, 133112.
(23) Liao, Z. M.; Wu, H. C.; Kumar, S.; Duesberg, G. S.; Zhou, Y. B.; Cross, G. L. W.; Shvets, I. V.; Yu, D. P. Large Magnetoresistance in Few Layer Graphene Stacks with Current Perpendicular to Plane Geometry. *Adv. Mater.* **2012**, *24*, 1862−1866.
(24) Ramasubramaniam, A.; Naveh, D.; Towe, E. Tunable band gaps in bilayer transition-metal dichalcogenides. *Phys. Rev. B* **2012**, *84*, 205325.
(25) Li, K. K.; Zhan, W.; Lee, Y. H.; Lin, Y. C.; Chang, M. T.; Su, C. Y.; Chang, C. S.; Li, H. Y.; Shi, Y.; Zhang, H.; Lai, C. S.; Li, L. J. Growth of Large-Area and Highly Crystalline MoS_2 Thin Layers on Insulating Substrates. *Nano Lett.* **2012**, *12*, 1538−1544.
(26) Lee, Y. H.; Zhang, X. Q.; Zhang, W.; Chang, M. T.; Lin, C. T.; Chang, K. D.; Yu, Y. C.; Wang, J. T. W.; Chang, C. S.; Li, L. J.; Lin, T. W. Synthesis of Large-Area MoS_2 Atomic Layers with Chemical Vapor Deposition. *Adv. Mater.* **2012**, *24*, 2320−2325.
(27) Qiu, H.; Pan, L. J.; Yao, Z. N.; Li, J. J.; Shi, Y.; Wang, X. R. Electrical characterization of back-gated bi-layer MoS_2 field-effect transistor and the effect of ambient on their performances. *Appl. Phys. Lett.* **2012**, *100*, 123104−1−3.
(28) Nguyen, L. N.; Lin, M. C.; Chen, H. S.; Lan, Y. W.; Wu, C. S.; Chang-Liao, K. S.; Chen, C. D. Photo-response of a nanopore device with a single embedded ZnO nanoparticle. *Nanotechnology* **2012**, *23*, 165201.
(29) Reed, M. A.; Zhou, C.; Deshpande, M. R.; Muller, C. J.; Burgin, T. P.; Jones, L., II; Tour, J. M. The Electrical Measurement of Molecular Junctions. *Ann. N. Y. Acad. Sci.* **1998**, *852*, 133.
(30) Liao, Z. M.; Liu, K. J.; Zhang, J. M.; Xu, J.; Yu, D. P. Photovoltaic effect and charge storage in single ZnO nanowires. *Appl. Phys. Lett.* **2008**, *93*, 023111.
(31) Fan, Z.; Lu, J. G. Electrical properties of ZnO nanowire field effect transistors characterized with scanning probes. *Appl. Phys. Lett.* **2005**, *86*, 032111.
(32) Schmidt, O. G.; Denker, U.; Eberl, K.; Kienzle, O.; Ernst, F.; Haug, R. J. Resonant tunneling diodes made up of stacked self-assembled Ge/Si islands. *Appl. Phys. Lett.* **2000**, *77*, 4341.
(33) Schuberth, G.; Abstreiter, G.; Gornik, E.; SchäfBer, F.; Luy, J. F. Resonant tunneling of holes in Si/Si_xGet_{1-x} quantum-well structures. *Phys. Rev. B* **1991**, *43*, 2280.
(34) Hinnemann, B.; Nørskov, J. K.; Topsøe, H. A Density Functional Study of the Chemical Differences between Type I and Type II MoS_2-Based Structures in Hydrotreating Catalysts. *J. Phys. Chem. B* **2005**, *109*, 2245.
(35) Ghatak, S.; Pal, A. N.; Ghosh, A. Nature of Electronic States in Atomically Thin MoS_2 Field-Effect Transistors. *ACS Nano* **2011**, *5*, 7707−7712.
(36) Smit, G. D. J.; Rogge, S.; Klapwijk, T. M. Enhanced tunneling across nanometer-scale metal−semiconductor interfaces. *Appl. Phys. Lett.* **2002**, *80*, 2568.
(37) Kraya, R. A.; Kraya, L. Y. The role of contact size on the formation of Schottky barriers and ohmic contacts at nanoscale metal-semiconductor interfaces. *J. Appl. Phys.* **2012**, *111*, 064302.
(38) Han, S. Y.; Lee, J. L.; Pearton, S. J. Electrical properties of nanoscale Au contacts on 4H-SiC. *J. Vac. Sci. Technol. B* **2009**, *27*, 1870.
(39) Britnell, L.; Gorbachev, R. V.; Geim, A. K.; Ponomarenko, L. A.; Mishchenko, A.; Greenaway, M. T.; Fromhold, T. M.; Novoselov, K. S.; Eaves, L. Resonant tunnelling and negative differential conductance in graphene transistors. *Nat. Commun.* **2013**, *4:1794*, 1−5.
(40) Nguyen, H. S.; Vishnevsky, D.; Sturm, C.; Tanese, D.; Solnyshkov, D.; Galopin, E.; Lemaître, A.; Sagnes, I.; Amo, A.; Malpuech, G.; Bloch, J. Realization of a Double-Barrier Resonant Tunneling Diode for Cavity Polaritons. *Phys. Rev. Lett.* **2013**, *110*, 236601.
(41) Li, X.; Zhang, F.; Niu, Q. Unconventional quantum hall effect and tunable spin hall effect in MoS_2 trilayers. *Phys. Rev. Lett.* **2013**, *110*, 066803.
(42) Harper, P. G. Anomalous effective mass in MoS_2. *J. Phys. C: Solid State Phys.* **1974**, *7*, 1247.
(43) Peelaers, H.; Van de Walle, C. G. Effects of strain on band structure and effective masses in MoS_2. *Phys. Rev. B* **2012**, *86*, 241401(R).